AIAA 99-0536 An Effectiveness Study of F-15 Forebody Flow Analysis Using *Cobalt*₆₀

K. E. Wurtzler Computational Sciences Branch Air Vehicles Directorate Air Force Research Laboratory Wright-Patterson AFB, OH

AN EFFECTIVNESS STUDY OF F-15 FOREBODY FLOW ANALYSIS USING COBALT₆₀

Kenneth E. Wurtzler*
Air Force Research Laboratory
Air Vehicles Directorate
WPAFB Ohio 45433-7913

ABSTRACT

A feasibility study of numerically modeling the asymmetrical flow on the F-15 forebody at high angles of attack and various forebody vortex control methods is presented. Emphasis is centered on the application of an unstructured, parallel flow solver for quick solution turnaround time. A full-scale F-15 forebody was modeled initially as completely symmetrical and then with a small, geometric imperfection near the tip. After the resultant asymmetry was modeled, two different strake planforms were modeled and their effects were Cobalt₆₀, an unstructured, parallel, implicit Navier-Stokes flow solver was used to calculate the flow. Four unstructured grids were constructed for the study. An initial grid resolution study was accomplished with boundary layer spacings of 0.001" and 0.0005". The clean forebody grid and the asymmetrical forebody grid each consisted of 1.5 million tetrahedra. The forebody with strakes grid was composed of 2.4 million tetrahedra. The forebody with tabs grid consisted of 1.8 million tetrahedra. Angles of attack ranged from 40° to 62°. The freestream Mach of 0.08 was extremely low due to wind-tunnel restrictions of the comparison data. Comparisons with experimental data show the flow solver performed extremely well in capturing the induced asymmetry. Numerical results for the vortex control methods show that the 10" strakes performed better than the tabs due to their broader influence.

This paper is declared a work of the U.S. Government and is not subject to copyright protection in the United States.

NOMENCLATURE

C₁ = body-axis rolling moment, roll left positive

C_m = body-axis pitching moment, nose up

C_n = body-axis yawing moment, nose left positive

C_p = pressure coefficient α = angle of attack, deg.

angle of sideslip (nose left positive), deg.

S = wing area (reference area), ft²
MAC = mean aerodynamic chord, ft
b = wing span (reference length), ft

INTRODUCTION

The state of the art in the numerical simulation of aircraft is generally limited to steady-state analysis of complete aircraft or unsteady analysis of simple geometries or aircraft components. Grid generation and geometry modeling has matured to the point where aircraft with weapons and detailed geometric complexity can be modeled. Further advancement to an analysis of viscous, unsteady aerodynamics of a complete aircraft requires large amounts of computer time due to the large number of grid points and the slow advancement of the solution process.

Research into the area of high angle-of-attack aerodynamics has been dominated by experimental testing. Initial wind-tunnel tests investigated the impact of different forebody shapes on the vortical flow field structure shedding from the nose. Traditional fighter forebody shapes of a slender nose (F-15, F-18) as well as newer, sharp-edged forebodies (F-117) were evaluated. Subsequent research looked into controlling the shedding

^{*} Aerospace Engineer, Computational Sciences Branch

vortices for optimal aerodynamic benefit. flight envelopes being expanded due to changing tactics and engineering ability, fighter aircraft were designed and expected to fly at higher angles of attack and maintain directional control. However, while pitching to high angles of attack, the vertical tails become surrounded by turbulent, dead air and are limited in their directional control capability. Therefore, relatively small side forces on the nose, even at zero sideslip, can dominate directional stability, creating large yawing moments. These small side forces are a result of asymmetrical shedding of the forebody vortices. Small surface imperfections such as radome gaps, dents, and sharp paint depth mismatches can affect the strength and path of one of the vortices. The resultant net yawing moment can then increase and the aircraft becomes unstable. This condition of an aircraft experiencing severe yawing moments at high angle of attack flight is called nose-slice departure. It is an unsteady phenomenon which can be catastrophic.

Once the basic understanding of forebody flow asymmetry and its ramifications was accomplished, the research emphasis shifted to finding actions and procedures that could prevent or lessen the asymmetry or even manipulate the flow for directional control. Geometric or passive flow control treatments, such as strakes and vanes, were evaluated as were pneumatic or active flow control techniques, consisting of blowing and suction^{1,2}. The majority of this work was either wind-tunnel experiments or flight tests. Tunnel experiments validated basic concepts and ideas but were limited to sub-scale models and simple geometries. NASA managed the High Alpha Research Vehicle Program (HARV) which utilized an F-18 aircraft with geometric forebody modifications for better control at high angle of attack flight³⁻⁵. The Air Force conducted pneumatic experiments on the X-29 and F-16 aircraft⁶ with a similar objective of forebody vortical flow control. Both programs were supported by wind-tunnel tests of innovative ideas and techniques. The overall result of these two programs was that the ability to maintain directional stability at high angles of attack was possible with both geometric and pneumatic techniques. these results were for individual aircraft and could not be generalized. Also, since these programs focused on the aerodynamic result, issues dealing with system integration and fleet modification were to be resolved by each operational command.

Computational research has been focused on the basic understanding of vortical flows shedding from simple geometries such as ogive cylinders, bodies of revolution, and wing/fuselage shapes^{7,8}. Previous computer resource limitations constrained these investigations to steady-state flow and fixed angles of attack. The majority of the research centered on what is needed in a flow solver to accurately capture the vortical flows. Since the vortex shedding from a slender forebody is viscously dominated, a Navier-Stokes flow solver is needed to accurately capture the resulting flow. To capture vortex asymmetry, full forebodies have to be modeled along with an induced imperfection. Several methods were investigated⁹⁻¹⁴ on how to accomplish this and it is now possible to numerically model such asymmetry. However, for sharp-edged geometries, an Euler flow solver is adequate to simulate the flow since the creation of the vortices is caused by the sharp edge. cumulative result of this work showed that computational analysis was capable of capturing the physics of forebody vortical flows and could predict vortex asymmetry from geometric disturbances.

As the technology pushed towards controlling the forebody vortices for directional control, the computational research community followed with analyses of both passive and active flow control methods¹⁵. Specifically, the Air Force investigated both geometric 10 and pneumatic flow control 16 methods on the Fighter Lift and Control (FLAC) Program¹⁷. With the FLAC being a sharp-edged forebody, Euler methods were used to simulate the flow. Strake sizing and placement were investigated as were various pneumatic blowing coefficients. Comparisons with wind-tunnel results were in good agreement. For slender forebody shapes, a fully viscous analysis is required which increases grid points and needed computer time. This limits analysis capability to aircraft components and simple aerodynamic flows.

NUMERICAL PROCEDURE

Overview of Cobalt₆₀

Cobalt₆₀ is a parallel, implicit unstructured flow solver developed by the Computational Sciences Branch of the Air Force Research Laboratory¹⁹. Godunov's first-order accurate, exact Riemann method²⁰ is the foundation of Cobalt₆₀. Second-order spatial accuracy, second-order accurate

implicit time stepping, viscous terms and turbulence models have been added to this procedure. $Cobalt_{60}$ uses a finite-volume, cell-centered approach. Arbitrary cell types in two or three dimensions may be used, and a single grid may be composed of a variety of cell types. Information on the calculation of inviscid and viscous fluxes and the dissipation in $Cobalt_{60}$ is reported in Strang¹⁹. Two one equation turbulence models have been implemented in $Cobalt_{60}$, the Spalart-Allmaras²¹ model and the Baldwin-Barth model²².

The implicit algorithm in *Cobalt*₆₀ was implemented and demonstrated by Tomaro²³ in 1997. The implicit algorithm resulted in a 5-10x speed up over the original explicit algorithm with only a 10 percent increase in memory required. Inviscid flows are simulated with CFL numbers of one million. However, turbulent flows severely limited the CFL for this implicit algorithm. A further addition to the original implicit algorithm, reported by Strang¹⁹, removed the CFL limit for viscous flows, allowing CFL numbers of one million on most problems. This modified implicit algorithm resulted in a 7-10x speed up in convergence over the original explicit code for viscous flows.

The development of the parallel version of *Cobalt*₆₀ was reported by Grismer²⁴. Domain decomposition is the basis for the parallel code. Each processor operates on a subsection (zone) of the original grid. Information is passed between processors using the Message Passing Interface (MPI) library routines. *Cobalt*₆₀ has been implemented and tested on IBM SP2's, Cray T3E's and SGI Origin 2000's. The resulting speed up of *Cobalt*₆₀ is often "superscalable"; the speed up factor is greater than the number of processors used.

Flow Conditions

Flow conditions were taken from the wind tunnel test conditions²⁶. The dynamic pressure was 10 psf. The corresponding flow velocity was 92 ft/sec with the Reynolds number reaching nearly 50,000/in. The input to *Cobalt*₆₀ required a Mach number of 0.082 and proper pressure and temperature values to get a similar Reynolds number. The reported Reynolds number from *Cobalt*₆₀ was 49,464/in. Flow was assumed to be laminar throughout the domain. The extremely low Mach number caused a very slow convergence rate. Convergence was reached on the order of 3,000-

4,000 iterations but several runs were carried to 10,000 iterations to check for any oscillations in the flow. None were discovered. Figure 1 shows convergence of y+, Figure 2 shows convergence of density residuals, and Figure 3 shows convergence of body forces.

Body Geometries and Grids

The F-15 forebody with four different tip geometries was modeled to match the corresponding geometry from the wind tunnel test²⁶. The four geometries were: clean, bump, bump with strakes, and bump with tabs. The wind tunnel test used F-15 production fleet radomes. The aft end was blunt and supported the model balance rig as shown in Figure 4. The length of the full-scale forebody section was 13.4'. Two grids with initial cell spacing of 0.001" and 0.0005" on a bump geometry were utilized for a grid resolution study to begin the analysis. The grid generation package of GridTool and VGRIDns²⁷ was Subsequent to that study, the clean forebody was modeled with 1.5 million cells in an unstructured, tetrahedral grid. The bump grid consisted of 1.6 millions cells. The bump was modeled on the lower left quadrant of the forebody, near the apex, by creating a small ridge of 0.3" maximum height on the surface. The bump with strakes grid contained 2.4 million cells. The strakes were modeled as thin wedges with thickness (Figures 5). Each strake was 10" long with a width of 1". The bump with tabs grid consisted of 1.8 million cells. The tabs consisted of the first inch of the strakes with the same width (Figure 5). Cells were clustered near the strakes and tabs, accounting for the larger grid size. This clustering is shown in Figure 6. Far field boundaries for all grids were 10 forebody lengths away

Code Specifications

Cobalt₆₀ allows the specification of a variety of boundary conditions²⁵. For the F-15 forebody simulations, the farfield was set to a modified Riemann invariant method. The surfaces of the body were adiabatic no-slip walls. Cobalt₆₀ was run in a laminar mode due to the low Reynolds number. Cobalt₆₀ was run in parallel on an IBM SP2 at the CEWES Major Shared Resource Center. For each run, the number of nodes used was varied. For most of the runs, 48 nodes were utilized which gave a

timing of 13.2 µsec/cell/iteration. Several runs utilizing 140 nodes took 4.2 µsec/cell/iteration. For a grid on the order of 2 million cells, this amounts to 26.2 sec/iteration for 48 nodes and 8.4 sec/iteration for 140 nodes.

RESULTS

All moments are resolved at the F-15's Aerodynamic Reference Point at FS 557.173, WL 116.173, and BL 0 to match the wind tunnel data. All force and moment data presented in this paper are in body-axis system and are relative to the Aerodynamic Reference Point. All aerodynamic coefficients were calculated based on the standard F-15 dimensions with $S=608 {\rm ft}^2$, MAC = 15.94 ft and $b=42.8 {\rm ft}$.

The force and moment data that were acquired used only the first 12 ft of the F-15 forebody. This causes the resultant data to be lower in magnitude due to the absence of the remaining forebody. However, the characteristics of the data should be representative of the forebody's contribution to the overall aerodynamics at high angles of attack where previous tests²⁸ have shown the forebody to dominate yaw characteristics. With control of the yawing moment being one of the primary research objectives, this is suitable for analysis.

Plots of pressure coefficient on the surface are compared directly with the wind tunnel data. The pressure coefficient is defined as follows:

$$C_{p_{(local)}} = \frac{\left(P_{local} - P_{\infty}\right)}{Q_{\infty}}$$

The test data was gathered from 256 pressure ports on the forebody (8 rows of 32 ports). This test data was then smoothed in the visual results. The color spectrum of the $Cobalt_{60}$ results is designed to match the experimental data. It is close to but not an exact match in the middle of the color spectrum due to some non-linearity in the tunnel color spectrum. However, the range of indices is exact. The view of all the surface plots is looking at the forebody. The definitions of right and left are from the **pilot's** point of view.

The first results discussed will be a grid resolution study. Computational results on the clean

forebody will be discussed next. Following that, the initial comparison with the experimental data is accomplished. The computational analysis of the different control devices is next followed by a discussion of the ease of application of *Cobalt*₆₀.

Grid Resolution Study

Since the control of the number of cells in an unstructured, tetrahedral grid is virtually impossible, grid resolution focused on the height of the first cell off the solid surface. Initial cell height can be explicitly stated in the grid generator package along with the stretching rate and number of cells in the boundary layer. The boundary layer contained 15 cells. The grid resolution study was conducted at the flow conditions of Mach = 0.082 and angle of attack of 40° .

The two different grid spacings reveal that a smaller first-cell height does affect both the pressure (inviscid) component and the friction (viscous) component of the values. The bump case had a 1.4% increase in the pressure component and an 11% increase in the friction component for pitching moment going from the 0.001" to 0.0005" cell height. The strake case had similar increases. For vawing and rolling moments, the increase is much greater, on the order of 50-100%. With the yawing and rolling moments showing the most instability, this variation is greater than is tolerable for results. With the small scale of the flow features and geometry, the vortices that are formed at the bump and control devices can be captured better with the tighter spacing. In Figure 7, pressure coefficient is shown on the same geometry with the different cell heights. The extent of surface area affected by the low pressure region is the same in both cases. However, the intensity of the low pressure region is increased in the 0.0005" case. From this analysis, the spacing of 0.0005" was chosen for all future grids.

Computation of 'Clean' Forebody

The flow over the clean forebody was simulated on two different grids. A symmetrical grid, which covered just one half of the forebody and then reflected about the y=0 plane, was evaluated first. A boundary condition of slip, tangential flow is assigned to the symmetry plane. With the clean

forebody being symmetrical, this is an exact numerical duplication of that. For this case, C_n was within the range of machine zero.

The second study was to grid the entire forebody with tetrahedra, which will be the method used on the remainder of the cases. Even though the surface triangulation might be symmetric about the symmetry plane due to the grid generation techniques, the resultant volume grid may not maintain grid symmetry. Thus, even though the geometry is 'numerically' symmetric, the numerical answer produced slightly asymmetrical results in C_n. However, this is not quantifiable in terms of identifying a geometric cause, such as a bump or gap. When compared to the bump and strake cases, this value of C_n was several orders of magnitude lower and will be disregarded in the results. Strict attention must be maintained in regard to keeping surface triangulation as isotropic as possible in order not to induce surface imperfections in the grid.

Validation: Forebody with Bump

The purpose of the validation is to compare the computational data with the experimental data at high angles of attack and beta conditions to assess the capability of the computational analysis to adequately capture the relevant flow physics. A secondary purpose is to determine the adequacy of the asymmetric geometry in the computational analysis to reproduce the experimental asymmetry. Static yawing moments are available for comparisons at $40^{\rm o}$ and $62^{\rm o}$ α and $0^{\rm o}$ β (Table 1). Plots of surface C_p are used for comparisons of selected cases where the experimental results were presented as such.

A bump was modeled on the lower left portion of the forebody by physically raising a grid line off of the surface database. This created a ridge that spanned 90° from bottom center to left horizontal. This did not exactly match any of the bumps or gaps that were created for the wind tunnel test. It is an example of a gap or paint-gap that has been documented in the wind tunnel report and is located in a similar position. Its purpose is to create a measurable asymmetric geometry imperfection that can be used as a baseline in the computational analysis. The location was kept near the tip for two reasons. First, this is where the impact from bumps

or gaps is the greatest and can affect all directional characteristics. Second, the experimental set-up confined its bumps and gaps to this same area.

The first comparison of static yawing moment is shown in Table 1 for 0° β. At 40° α, both the computational and experimental data show a negative yawing moment. As the angle of attack increases to 62°, the yawing moment increases in magnitude in both cases by the same amount. Since the 'bump' geometries are not exact, the results will not necessarily match. However, trends and delta values can be determined. The addition of the 10" strakes in both cases reduces the yawing moment substantially at both angles of attack. Since the strakes are very similar and their influence overshadows the bump effects, the results show better agreement here. The tab data is shown for comparison with the numerical strake case for the effect of size and shape.

α	Bump	Bump	Strake	Strake	Tab
	EXP	CFD	EXP	CFD	CFD
40	-0.00068	-0.00077	-0.00039	-0.00032	N/A
62	-0.0141	-0.0126	-0.007	-0.0062	-0.008

Table 1. Comparison of Experimental and Computational Results of Eliminating Static Yawing Moment Offset Induced by Medium Bump at 0° β .

The test data available for comparison of the beta cases consists of plots of surface Cp on the bump forebody with and without strakes. At 62° α and 0° β , the influence of the bump can be seen in both the computational and experimental data (Figure 8). The stagnation region is evident on the underside centerline. As the flow accelerates around the forebody, low pressure regions are created. The bump side low pressure region is reduced due to its presence. As the flow reaches the adverse pressure gradient on the top half of the forebody, it separates into a pair of off-body vortices. This is exhibited in the prong-like features emanating from the tip. The shedding vortex is altered in its growth and its direction on the bump side. The yawing moment is negative due to the larger suction region on the windward side (Table 1), creating a nose right force.

When the strakes are added to this geometry (Figure 9), the flow is returned to more symmetrical behavior and the yawing moment is lessened considerably as seen in Table 1. The suction regions on both sides are evened out and controlled by the strakes. Additionally, flow symmetry is increased by the dominating vortices at the apex of the forebody, which shows the importance of that region in yaw control. At 20° β, the comparison between experimental and computational data shows good agreement even though the only experimental data available for this case involves 20" strakes (Figure 10). The regions with separation are accurately captured with the tight grid spacing and grid clustering near the strakes. As seen in both cases, the small pocket of high pressure on the underside of the leeward strake is evidence of the accurate capturing of the relevant flow physics in the computational analysis. The 10" strakes in the numerical case have a lesser impact on the tip vortices when compared to the 20" strakes in the experimental case.

From the cases discussed above, it is evident that the computational analysis performs as well as the experimental analysis in capturing the dominant flow physics. From these comparisons, it is also determined that the asymmetrical geometry used in the computational analysis is adequate for use as a baseline for further control device analysis.

Control Devices

The addition of control devices on the forebody is aimed at reducing the large, adverse yawing moments caused by geometric imperfections near the forebody tip. Their effect on other directional characteristics also has to be considered when evaluating their performance. Various physical attributes of the devices are shape, size, and location. The work described in this paper evaluated only the size and shape difference of two control devices.

The two devices evaluated are a 10" long, 1" wide strake that is tapered near the tip. The second is a tab that consists of the first inch of the strake. The front tips of both devices rest in the same location. Both are located 90° down from the centerline on both sides.

At 62° α , when the forebody is put through a positive and negative beta sweep, the full impact of

the strakes and tabs on the static yawing moment can be evaluated (Figure 11). The bump case produces a nose right yawing moment at all sideslip angles, with the largest moment at -10° β and decreasing down to 20° β. The experimental data from similar cases of gaps and bumps put in the same location produced similar results at 60° α^{26} . The 10" strakes improve the directional characteristics at this angle of attack by decreasing the magnitude of the yawing moment when compared to the bump case. The tabs produced mixed results throughout the beta sweep. At beta angles between -10° and 0° β , the tabs exhibit a favorable trend that dissolves at positive B. It is possible that the tabs are too small in comparison to the bump for their influence to dominate at higher beta angles.

A flow field analysis of streamlines and pressure isosurfaces for the 4 sideslip angles at 62° α is shown in Figures 12 - 15. At -10° β, high energy vortices emanating from the strakes control the flow near the tip. The vortices from the tabs are weaker and interfere less with the suction peaks. leeward side vortical production is greater with the strakes, being enough to create a larger negative yawing moment than the tabs. At 0° β, the suction peak on the non-bump side is larger in the strake case. This imbalance is more pronounced at 10° and 20° β. The suction on the windward side is larger in the tab case while the strakes act more to even out the regions. Plus, the high energy vortices from the strakes provide a stabilizing influence over the bump asymmetry. This allows the effect of the sideslip angle to control the yawing moment. Plots of Cp at FS 125 and FS 145 for the 0° and 20° β are shown in Figures 16-19. At FS 125, the vortices emanating from the strakes are stronger at both beta angles. Further back at FS 145, the strake case has already returned to a balance at 0° β while the tab and bump cases exhibit a pressure imbalance. At 20° β, the influence of the forebody is diminished due to the large angle. All three cases show about the same pressure values. This again highlights the importance of the forward forebody region in effecting any change in vawing moment.

|--|

-10°	0.0467	0.0472	0.0470
$0_{\rm o}$	0.0569	0.0554	0.0527
10°	0.0624	0.0557	0.0601
20°	0.0837	0.0536	0.0679

Table 2. Effectiveness of Two Different Forebody Control Devices on Pitching Moment (C_m) .

The effect of these control devices on the static pitching moment has to be considered along with their impact on lateral directional stability. At sideslip angles, any increase in nose-up effect can be detrimental. The strake does an extraordinary job of limiting an increase in C_m (Table 2). When compared to the bump case, C_m is lower for each angle of attack case. The tab is greater than the strake case but less than the bump case. The addition of the control devices limits the vertical growth of the suction region on the sides of the forebody.

A top and front view of surface Cp is shown in Figures 20 and 21 for the strake case and the bump case at 10° β . The windward side suction peak encroaches farther up on the forebody on the bump case. The strakes lessen the pressure magnitude in the suction regions and the vortices depart from the body sooner. This may account for the higher static pitching moment for the bump case.

The balancing of the direction and strength of the tip vortices by the control devices reduces the rolling moment, with the tabs providing greater reduction (Table 3). The imbalance of the low pressure regions on the sides of the forebody is lessened with the control devices.

β	Bump	Strakes	Tab
-10°	0.000099	0.000015	0.000061
$0_{\rm o}$	-0.000005	-0.000004	-0.000009
10°	-0.000105	-0.000097	-0.000118
20°	-0.000293	-0.000119	-0.000188

Table 3. Effectiveness of Two Different Forebody Control Devices on Rolling Moment (C_1) .

Oil flow analysis also demonstrates the ability of the control devices to alter the flowfield in a favorable manner. As seen in Figures 22-25, the direction of the forebody vortices are tracked for the bump, tab, and strake cases. The strakes actually provide a straightening effect to the surface flow at all beta angles, providing a favorable condition for reduced rolling moment. They also push the tip vortices away from the centerline which will be a more stable flowfield at all conditions.

Ease of Application

An analysis of the computational resources and application tools has shown that a turnaround time of 2 to 3 days is possible per case. Most of this time is related to the extremely low Mach number and the corresponding large number of iterations needed for convergence. $Cobalt_{60}$ does not incorporate any preconditioning methods to increase the rate of convergence for nearly incompressible flows.

As in any computational analysis, several separate types of work make up the total turnaround time: grid generation, flow solution, and result analysis. By utilizing the benefits of unstructured grids, the grid generation took less than 2 hours per geometry with GridTool and VGRIDns. Altering strake size or location on the CFD geometry model can be accomplished quickly and efficiently. With the comparisons described above, the quality of the viscous grid is deemed exceptional when combined with the robustness of $Cobalt_{60}$.

With the parallel ability in *Cobalt*₆₀, it is possible to get solution turnaround in 1 day if a sufficient number of nodes is available. Some of the parallel runs utilized 140 nodes on a massively parallel machine. The adaptability of *Cobalt*₆₀ to run on different computer platforms also increases the number and type of machines available for computing, whether massively parallel or networked together. This application points to an ability to achieve same day Navier-Stokes analysis of component aerodynamics. Aerodynamic analysis, from grid generation to solution, of full aircraft is plausible in a 1 week time frame. A grid of 7-8 million cells would be needed for an accurate analysis of control devices on a full aircraft.

CONCLUSIONS

An analysis using an unstructured parallel CFD method to investigate flowfield asymmetries and

possible control methods on an F-15 forebody was accomplished. The comparison of qualitative and quantitative results has shown very good agreement with the full-scale wind tunnel results for the 10" strakes. Two control devices of different size were evaluated using CFD. An analysis of the results determined that the 10" strakes performed better than the tab when all directional characteristics were taken into account. The strakes reduced the adverse effects of the bump and created minimal adverse effects of their own. Quick turnaround time was achieved for each case by utilizing the parallel capability of Cobalt₆₀. The ability to do preliminary design analysis with unstructured CFD has been shown with accuracy and efficiency taken into account.

ACKNOWLEDGEMENTS

I would like to thank the ASC MSRC at Wright-Patterson AFB, OH and the CEWES MSRC at Vicksburg, MS for the use of their parallel computers and support. Specifically, the code was run on IBM SP2 machines with 230 nodes capacity at each location. Also, the support of the *Cobalt*₆₀ development team and the BMC is greatly appreciated.

REFERENCES

- Malcolm, G.N. and Ng T.T, "Forebody Vortex Control as a Complement to Thrust Vectoring," AIAA 90-1851.
- Boalbey, R.E., Ely, W.L., and Robinson, B.A.,
 "A Sensitivity Study for Pneumatic Vortex Control on a Chined Forebody," AIAA 93-0049.
- Fisher, D.F., Del Frate, J.H., and Richwine, D.M., "In-Flight Visualization Characteristics of the NASA F-18 High Alpha Research Vehicle at High Angles of Attack," SAE Paper 892222, September 1989.
- Schiff, L.B., Cummings, R.M., Sorenson, R.L. and Rizk, Y.M., "Numerical Simulation of High-Incidence Flow over the F-18 Fuselage Forebody," AIAA 89-0339.
- 5. Cummings, R.M., Rizk, Y.M., Schiff, L.B. and Chaderjian, N.M., "Navier-Stokes Predictions of

- the Flowfield Around the F-18 (HARV) Wing and Fuselage at Large Incidence," AIAA 90-0099, January 1990.
- Lemay, S.P., Sewell, W.G., and Henderson, J.F., "Forebody Vortex Flow Control on the F-16C Using Tangential Slot and Jet Nozzle Blowing," AIAA 92-0019, January 1992.
- Schiff, L.B., Degani, D., and Gavali, S., "Numerical Simulation of Vortex Unsteadiness on Slender Bodies of Revolution at Large Incidence," AIAA 89-0195, January 1989.
- 8. Ghaffari, F., "On the Vortical-Flow Prediction Capability of an Unstructured-Grid Euler Solver," AIAA 94-0163, January 1994.
- Degani, D. and Schiff, L.B., "Numerical Simulation of the Effect of Spatial Disturbances on Vortex Asymmetry," AIAA 89-0340, January, 1989.
- Siclari, M.J. and Marconi, F., "The Computation of Navier-Stokes Solutions Exhibiting Asymmetric Vortices," AIAA 89-1817, June, 1989.
- 11. Degani, D., "Numerical Investigation of the Origin of Vortex Asymmetry," AIAA 90-0593, January, 1990.
- Degani, D., Schiff, L.B., and Levy, Y., "Physical Considerations Governing Computation of Turbulent Flows Over Bodies at Large Incidence," AIAA 90-0096, January, 1990.
- 13. Siclari, M.J., "Asymmetric Separated Flows at Supersonic Speeds," AIAA 90-0595, January, 1990.
- Hartwich, P.M., Hall, R.M., and Hemsch, M.J., "Navier-Stokes Computations of Vortex Asymmetries Controlled by Small Surface Imperfections," AIAA 90-0385, January, 1990.
- Tavella, D.A., Schiff, L.B., and Cummings, R.M., "Pneumatic Vortical Flow Control at High Angles of Attack," AIAA 90-0098, January, 1990.

- Wurtzler, K., "Numerical Analysis of a Chined Forebody with Asymmetric Strakes," AIAA 93-0051, January, 1993.
- 17. Wurtzler, K., "Numerical Analysis of a Chined Forebody with Asymmetric Blowing," AIAA 94-0171, January, 1994.
- Alexander, M.G. and Rogers, L.W., "Flow Visualization of the 2.7% Fighter Lift and Control (FLAC) Configuration with Forebody Strakes and Other Control Effectors," WL-TR-93-3008, February, 1993.
- Strang, W. Z., Tomaro, R. F., and Grismer, M. J., "The Defining Methods of *Cobalt₆₀*: A Parallel Implicit, Unstructured Euler/Navier-Stokes Flow Solver," AIAA 99-0786, January 1999.
- Godunov, S. K., "A Finite Difference Method for the Numerical Calculation of Discontinuous Solutions of Equations of Fluid Dynamics," Sbornik Mathematics, Vol 47, p. 271-290, 1959.
- 21. Spalart, P. R. and Allmaras, S. R., "A One-Equation Turbulence Model for Aerodynamic Flows," AIAA 92-0439, January 1992.
- Baldwin, B. S. and Barth, T. J., "A One-Equation Turbulence Transport Model for High Reynolds Number Wall-Bounded Flows," NASA TM 102847, August 1990.
- Tomaro, R.F., Strang, W.Z. and Sankar, L. N., "An Implicit Algorithm for Solving Time Dependent Flows on Unstructured Grids," AIAA 97-0333, January 1997.
- 24. Grismer M. J., Strang, W. Z., Tomaro, R. F., and Witzeman, F. C., "*Cobalt₆₀*: A Parallel, Implicit, Unstructured Euler / Navier-Stokes Solver," *Advances in Engineering Software*, Vol 29, No. 3-6, pp. 365-373, Apr-Jun 1998.
- 25. Strang, W.Z., "Parallel *Cobalt*₆₀ User's Manual," AFRL/VAAC, WPAFB, OH, August 1998.
- 26. Kay, J., Kloc, S., and Stowe, E., "High Angle of Attack Full-Scale F-15 Forebody Wind Tunnel

- Testing," Bihrle Applied Research, INC, BAR 97-4, June 1997.
- 27. Pirzadeh, S., "Three-Dimensional Unstructured Viscous Grids by the Advancing-Layers Method," *AIAA Journal*, Vol. 34, No. 1, January 1996, p. 43-49.
- Kay, J. and Ralston, J., "F-15E High Angle of Attack Study, Including Data Analysis, Aerodynamic Math Modeling and Simulation," BAR95-2, March 1995.

FIGURES

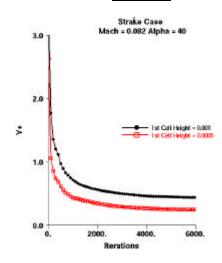


Figure 1. Convergence of y+.

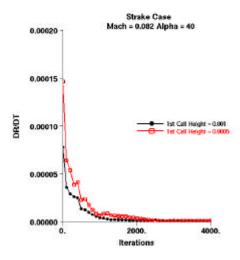


Figure 2. Convergence of density residual.

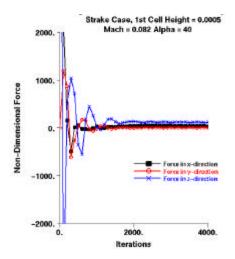


Figure 3. Convergence of body forces.

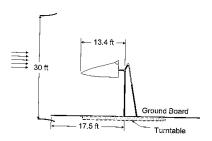
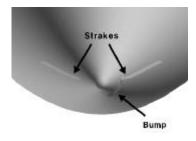


Figure 4. Wind tunnel test set-up.



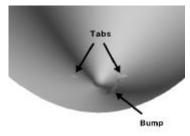


Figure 5. F-15 forebody with bump, strakes and tabs.

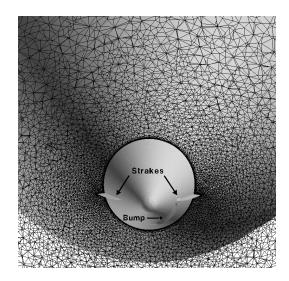


Figure 6. Close-up of F-15 forebody with bump and strakes with unstructured grid.

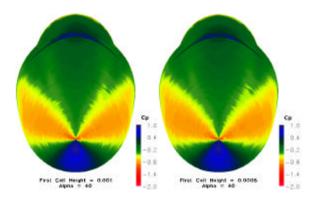


Figure 7. Plot of surface Cp on forebody with bump with initial cell height of 0.001'' (left) and 0.0005'' (right).

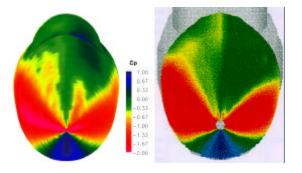


Figure 8. Plot of surface Cp with computational (left) and experimental (right) data on forebody with bump. $\alpha=62^{\circ}, \beta=0^{\circ}$.

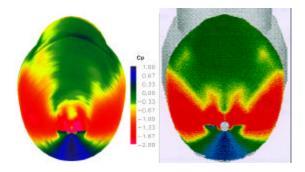


Figure 9. Plot of surface Cp with computational (left) and experimental (right) data on forebody with bump and 10" strakes. $\alpha=62^{\circ}$, $\beta=0^{\circ}$.

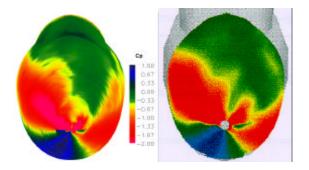


Figure 10. Plot of surface Cp with computational (left) and experimental (right) data on forebody with bump and 10"(CFD) and 20"(EXP) strakes. $\alpha = 62^{\circ}$, $\beta = 20^{\circ}$.

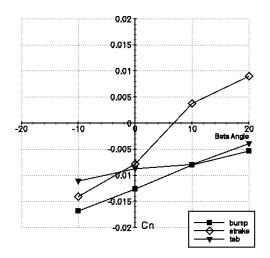


Figure 11. Effect of 10" strakes and tabs on directional characteristics of forebody.

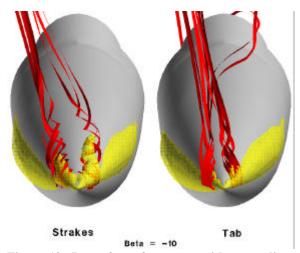


Figure 12. Isosurface of pressure with streamlines off control devices. $\beta = -10^{\circ}$.

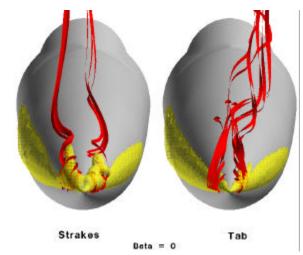


Figure 13. Isosurface of pressure with streamlines off control devices. $\beta = 0^{\circ}$.

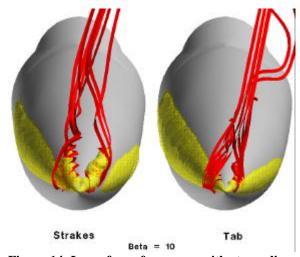


Figure 14. Isosurface of pressure with streamlines off control devices. $\beta=10^{\circ}$.

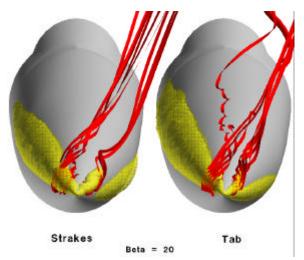


Figure 15. Isosurface of pressure with streamlines off control devices. $\beta = 20^{\circ}$.

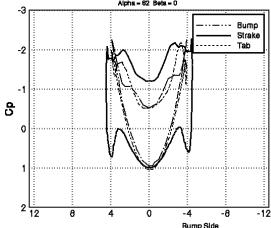


Figure 16. Plot of Cp values at FS 125. $\beta = 0^{\circ}$.

Bump Side

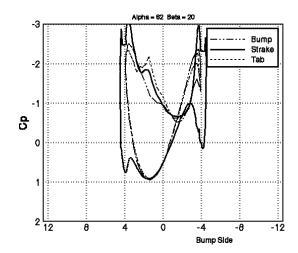


Figure 18. Plot of Cp values at FS 125. $\beta = 20^{\circ}$.

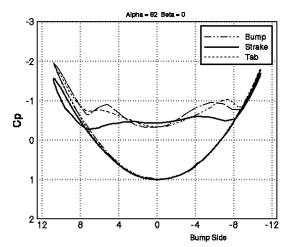


Figure 17. Plot of Cp values at FS 145. $\beta = 0^{\circ}$.

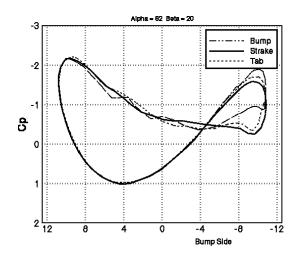


Figure 19. Plot of Cp values at FS 145. β =20°.

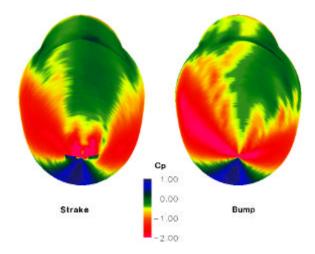


Figure 20. Surface Cp on strake and bump case. $10^{\circ}\,\beta$. Front view.

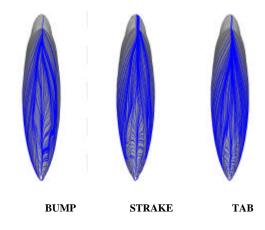


Figure 23. Oil flow for $\alpha=62^{o}$, $\beta=10^{o}$ case.

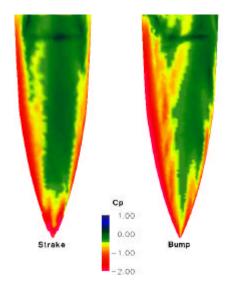


Figure 21. Surface Cp on strake and bump case. $10^{\rm o}~\beta.$ Top view.

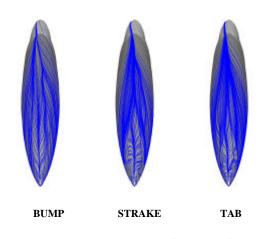


Figure 24. Oil flow for $\alpha=62^{o}$, $\beta=\text{-}10^{o}$ case.

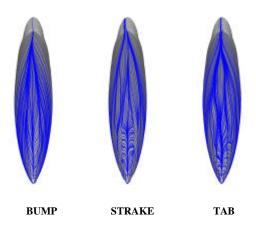


Figure 22. Oil flow for $\alpha=62^o$, $\beta=0^o$ case.

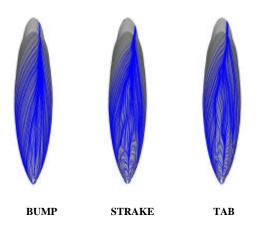


Figure 25. Oil flow for $\alpha=62^{o}$, $\beta=20^{o}$ case.